Three-dimensional multifluid modeling of atmospheric electrodynamics in Mars' dynamo region

Jeremy A. Riousset,[1] Carol S. Paty,[1] Robert J. Lillis,[2] Matthew O. Fillingim,[2] Scott L. England,[2] Paul G. Withers,[3] and John P. M. Hale[1]

Received 22 February 2013; revised 7 May 2013; accepted 8 May 2013.

[1] The interactions between Mars' unique crustal magnetic fields and upper atmospheric particles lead to the formation of currents in the ionospheric dynamo region. This work is specifically focused on the collisions between ions, electrons, and neutrals in the atmospheric column of Mars. The remanent fields embedded in the Martian crust generate a very rich magnetic topology with important variations in terms of geometry and amplitude. Here we present mesoscale, self-consistent, three-dimensional, multifluid simulations of Mars' ionospheric electrodynamics in the dynamo region (∼100–400 km altitude), where differential motions of ions and electrons occur. In particular, we develop and validate a new method through the study of simple, uniform magnetic geometries. Our results demonstrate the existence of a dynamo current in the Martian atmosphere, which depends on the magnitude of the applied magnetic field and the neutral wind speeds. The simulation outputs are analyzed from mathematical and physical perspectives to identify the dominant processes at work in the formation of this current. Both case studies presented in this paper are qualitatively and quantitatively consistent with theoretical estimates and confirm the validity of the model, hence laying the groundwork for future studies of Mars' atmosphere using this new approach.

Citation: Riousset, J. A., C. S. Paty, R. J. Lillis, M. O. Fillingim, S. L. England, P. G. Withers, and J. P. M. Hale (2013), Three-dimensional multifluid modeling of atmospheric electrodynamics in Mars' dynamo region, *J. Geophys. Res. Space Physics*, *118*, doi:10.1002/jgra.50328.

1. Introduction

[2] The Mars Global Surveyor mission ended the ongoing debate on the existence of a global magnetic field on the planet [*Nagy et al.*, 2004] and revealed the presence of small-scale magnetic anomalies caused by crustal remanent magnetism [*Acuña et al.*, 1999; *Connerney et al.*, 1999]. After the cessation of Mars' internal dynamo ∼4.1 Gyr age [*Jakosky and Phillips*, 2001; *Lillis et al.*, 2008], subsequent volcanic activity and impact history substantially altered these remanent fields, creating a very nonuniform magnetic topology, varying on a scale of ∼50–100 km [*Brain et al.*, 2003]. The complex magnetic topology of Mars leads to strong and weak, open and closed magnetic field regions in very close proximity, which strongly affect the behavior of the ionosphere. In this work, we focus on the atmospheric plasma interactions with the magnetic field $\vec{B}$ in Mars' ionospheric dynamo region (not to be confused with the now-extinct core geo-dynamo). The dynamo region is a region where electrons are magnetized and ions are not. We refer to a magnetized particle as an electron or an ion $\left(O_2^+, CO_2^+, \text{ or } O^+\right)$, whose gyropath is not notably perturbed by collisions with other charged or neutral particles. The upper and lower limits of this region on Mars usually range between 100 and 400 km depending on the values of the local magnetic field and electron, ion, and neutral densities.

[3] Their heights can be estimated by comparing the gyrofrequencies of O_2^+, the dominant ion, and electrons, to their respective collision frequencies with CO_2, the most abundant neutral. The gyrofrequency or cyclotron frequency Ω_α for a species α is given by its usual definition: $\Omega_\alpha = eB/m_\alpha$, where e and m_α are the elementary charge and the mass of the particle α, respectively. On the other hand, the electron-CO_2 and $O_2^+ - CO_2$ collision frequencies depend on altitude and are given as a function of the temperatures of electrons, ions, and neutrals in Table 1. Specifically, electrons are expected to be mostly demagnetized below the altitude defined by $\Omega_e = \nu_{e\text{-}CO_2}$, and magnetized above. Similarly, O_2^+ ions are expected to be magnetized above the altitude where their cyclotron frequency $\Omega_{O_2^+}$ is equal to their collision frequency with CO_2 $\left(\nu_{O_2^+\text{–}CO_2}\right)$ and demagnetized below. Together, these two altitudes form the a priori upper and lower boundaries of the dynamo region.

[1]School of Earth and Atmospheric Sciences, Georgia Institute of Technology, Atlanta, Georgia, USA.
[2]Space Sciences Lab, University of California, Berkeley, California, USA.
[3]Astronomy Department, Boston University, Boston, Massachusetts, USA.

Corresponding author: J. A. Riousset, Department of Earth and Atmospheric Sciences, Georgia Institute of Technology, Ford ES&T Building, 311 Ferst Drive, Atlanta, GA 30332, USA. (riousset@gatech.edu)

2169-9380/13/10.1002/jgra.50328

Table 1. Momentum Transfer Collision Frequencies (s^{-1}) for Ions-Neutrals and Electrons-Neutrals Interactions (From *Schunk and Nagy*, [2000, pp. 96–99])[a]

Species	Collision Frequency	Remark
	Ions-Neutrals	
$\nu_{O_2^+-CO_2}$	$5.63 \times 10^{-16} n_{CO_2}$	
$\nu_{CO_2^+-CO_2}$ [b]	$2.85 \times 10^{-17} n_{CO_2} T_r^{\frac{1}{2}} (1 - 0.083 \log_{10}(T_r))^2$	$T_r > 850$ K[c]
$\nu_{O^+-CO_2}$	$8.95 \times 10^{-16} n_{CO_2}$	
$\nu_{O_2^+-O}$	$2.31 \times 10^{-16} n_O$	
$\nu_{CO_2^+-O}$	$1.76 \times 10^{-16} n_O$	
ν_{O^+-O} [b]	$3.67 \times 10^{-17} n_O T_r^{\frac{1}{2}} (1 - 0.064 \log_{10}(T_r))^2$	$T_r > 235$ K [c]
	Electrons-Neutrals	
ν_{e-CO_2}	$3.68 \times 10^{-14} n_{CO_2} \left(1 + 4.1 \times 10^{-11} \lvert 4500 - T_e \rvert^{2.93}\right)$	
ν_{e-O}	$8.9 \times 10^{-17} n_O \left(1 + 3.6 \times 10^{-2} T_e^{\frac{1}{2}}\right) T_e^{\frac{1}{2}}$	

[a]Densities are in m^{-3}. Temperatures are in K.
[b]Resonant interactions.
[c] $T_r = \frac{T_i + T_g}{2}$

[4] For the case of a local, uniform, and radial planetary magnetic field of magnitude 20 nT with the atmospheric profiles illustrated in Figure 1, the dynamo region is expected to span between ∼150 and ∼225 km. This location is gray shaded on the left-hand side of Figure 2a, and the shading is extended to the right-hand side of the plot for the sake of comparison with the peak of the electron density.

[5] Previous modeling of Mars' ionosphere has focused on the interactions of the solar wind with Mars' atmosphere. At present, three distinct "classes" of models have been developed and used to study such interactions: (1) semikinetic (hybrid) models, which treat ions as particles and electrons as a neutralizing fluid [e.g., *Brecht and Thomas*, 1988; *Brecht and Ledvina*, 2010; *Kallio and Jarvinen*, 2012; *Modolo et al.*, 2012]; (2) single fluid, multispecies magnetohydrodynamic (MHD) models [e.g., *Ma et al.*, 2002, 2004], which use one continuity equation per species, but only one momentum equation for the plasma velocity; (3) multifluid, multispecies MHD models [e.g., *Sauer et al.*, 1997; *Harnett and Winglee*, 2006; *Harnett*, 2009], which use the

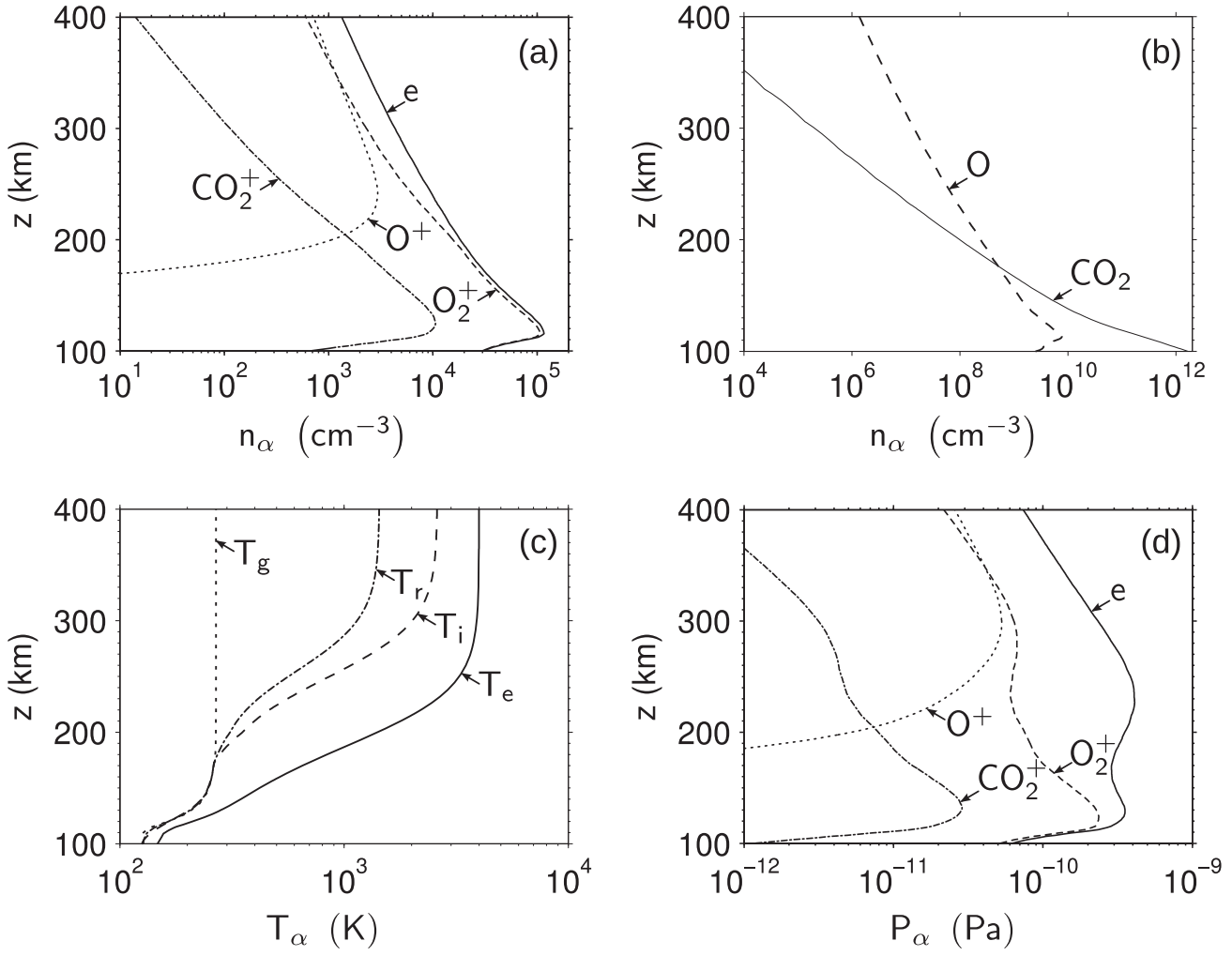

Figure 1. Initial profiles used for the simulation run presented in this paper. (a) Electron, O_2^+, CO_2^+, and O^+ density profiles (solid, dashed, dash-dotted, and dotted lines, respectively). (b) CO_2 and O neutral density profiles (solid and dashed lines, respectively). (c) Neutral (T_g), ions ($T_i = T_{O_2^+} = T_{CO_2^+} = T_{O^+}$), and electron ($T_e$) temperatures (solid, dashed, and dotted lines, respectively). (d) Electron, O_2^+, CO_2^+, and O^+ pressure profiles (solid, dashed, dash-dotted, and dotted lines, respectively). The pressure for each species α is calculated as $p_\alpha = n_\alpha k_B T_\alpha$.

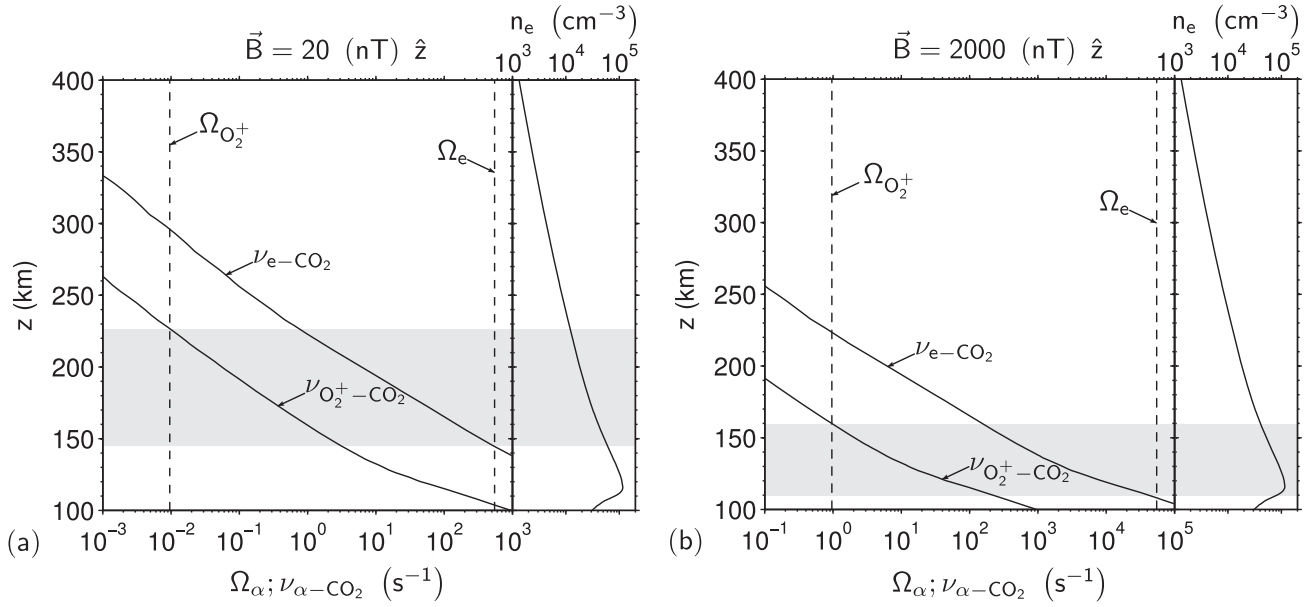

Figure 2. Estimated altitude of the dynamo region for a uniform magnetic field (a) $\vec{B} = 20$ nT $\hat{z}$, (b) $\vec{B} = 2000$ nT $\hat{z}$. Electron-CO_2 collision frequency (ν_{e-CO_2}), electron cyclotron frequency (Ω_e), O_2^+–CO_2 collision frequency $\left(\nu^+_{O_2} - CO_2\right)$, and O_2^+ cyclotron frequency $\left(\Omega_{O_2^+}\right)$ (panels' left-hand sides). Vertical electron density profiles at $t = 0$ s in the center of the model, compared to altitude a priori of the dynamo region (gray shading) (panels' right-hand sides). The dynamo region is bounded above by the altitude at which $\nu_{O_2^+-CO_2} \approx \Omega_{O_2^+}$ and below by the altitude at which $\nu_{e-CO_2} \approx \Omega_e$.

same MHD equations as the previous class but use one momentum equation per ion species. *Nagy et al.* [2004] and *Ledvina et al.* [2008] provide excellent reviews of the various models and of their respective fields and ranges of applicability. Indeed, *Ledvina et al.* [2008] emphasized the suitability of multifluid MHD models, such as the one developed in this paper, for collisional plasma and specifically in Mars' atmosphere. The salient specificities of the model introduced in section 2 lie in: (1) the direct modeling of the atmospheric resistivity via the collision frequencies and (2) the small size of the region relevant to our investigations, compared to the global models involved in simulating the effect of the solar wind on Mars' ionosphere.

[6] Here we present a novel modeling of the interactions between Mars' remanent crustal fields $\vec{B}$ and the three dominant ionospheric ions (O_2^+, CO_2^+, and O^+). Our results demonstrate that conduction currents $\vec{J}$ can develop in the dynamo region under the influence of the local magnetic field $\vec{B}$ due to the difference in the behavior of electrons and ions. The direction and magnitude of the dynamo currents depend on the properties of Mars' ionosphere and vary on a scale of a few tens or hundreds of kilometers. The present paper introduces a three-dimensional, multifluid model of Mars' lower ionosphere and lays the groundwork for the study of the effects on the dynamo current of: (1) the local magnetic field configuration, (2) the neutral wind direction and magnitude, and (3) the local ionospheric profiles (in particular, the effects of photoionization and electron impact ionization on the dayside and nightside ionospheres, respectively). The first stage of this work, namely the validation for simple magnetic configurations, is the central topic of this paper. Specific topographies including magnetic cusps and loops are investigated in a separate work (J. A. Riousset et al., in preparation, 2013). The next section (section 2) provides the details of the model, while a discussion of the development of ionospheric currents in the dynamo region due to the different behaviors of ions and electrons is given in section 3 and discussed in section 4. The key findings of this work are summarized in section 5.

2. Model Formulation

[7] In this section, we introduce the model used in the studies described in sections 3 and 4. The lack of symmetry in Mars' ionosphere and magnetic field makes it necessary to employ a 3-D model, and consequently, we use a 3-D Cartesian simulation domain spanning between –100 and 100 km, –50 and 50 km, 100 and 400 km along the *x*-, *y*-, and *z*-axes, respectively. Both observational data [e.g., *Brain et al.*, 2003, 2007] and modeling studies [e.g., *Purucker et al.*, 2000; *Cain et al.*, 2003; *Arkani-Hamed*, 2004] of Mars' crustal fields show spatial variations on the orders of a few tens of kilometers. Additionally, modeling studies of dayside and nightside ionospheric profiles [*Lillis et al*., 2011, 2012] show similar spatial variability. In view of these results, a simulation box with horizontal dimensions 200 km × 100 km is expected to enclose a region large enough to treat the effect of local magnetic fields and atmospheric profiles on ionospheric dynamics. For Martian crustal magnetic fields, the dynamo region as defined in section 1 remains consistently between 100 and 400 km altitude, providing us with an altitude range defining the simulation domain.

2.1. Initial Conditions and Altitude Profiles

[8] Although composed mainly of O_2^+, Mars' ionosphere also contains considerable amounts of CO_2^+ and O^+, and

some H^+ ions from the solar wind above ∼400 km [e.g., *Hanson et al.*, 1977; *Ma et al.*, 2002, 2004]. Considering the moderate size of the simulation domain, we assume small horizontal variations in the atmosphere, and therefore, we adopt horizontally uniform profiles at $t = 0$ s.

[9] The Mars Climate Database [*Lewis et al.*, 1999] provides insightful information about the Martian atmospheric composition under various conditions. In particular, the neutral density profiles reproduced in Figure 1b and those used by *Lillis et al.*'s [2012] model to derive the photoionization rates are retrieved from this database. Throughout this paper, we use modeled atmospheres corresponding to Mars year 24 dust opacities, moderate EUV fluxes, 0° latitude, 0° longitude, Northern autumnal equinox ($L_s = 180°$) for 2 P.M. local time. Specifically, the model of *Lillis et al.* [2012] employs a standard solar moderate UV spectrum, the aforementioned neutral density profiles of CO_2, O, CO, N_2O_2, and Ar, and the photoelectron impact parameterization of *Mendillo et al.* [2011] to derive the photoionization rates of CO_2 and O $\left(P_{\mathrm{ph}}^{\mathrm{CO_2,O}}\right)$, as a function of the altitude h. We employ a commonly used electron temperature profile $T_e(h)$ derived from Viking I measurements [*Hanson and Mantas*, 1988] combined with the empirical model of *Chen et al.* [1978], that allows us to calculate the effective recombination rate β_{eff} (in $\mathrm{cm^{-6}s^{-1}}$). The rate β_{eff} is taken to be the dissociative recombination rate of O_2^+ [e.g., *Lillis et al.*, 2009]:

$$\beta_{\mathrm{eff}} = \begin{cases} 1.95 \times 10^{-7} \left(\dfrac{300\ \mathrm{K}}{T_e}\right)^{0.7} & T_e < 1200\ \mathrm{K} \\ 1.73 \times 10^{-7} \left(\dfrac{300\ \mathrm{K}}{T_e}\right)^{0.61} & T_e \geq 1200\ \mathrm{K} \end{cases} \quad (1)$$

While other ion species are present, this reaction dominates the recombination of electron. The knowledge of the above quantities ultimately leads to the formulation of the following equation for electron number density profile [*Lillis et al.*, 2009]:

$$n_e(h) = \sqrt{\frac{P_{\mathrm{ph}}^{\mathrm{CO_2}} + P_{\mathrm{ph}}^{\mathrm{O}}}{\beta_{\mathrm{eff}}(T_e(h))}} \quad (2)$$

This expression gives us the electron density profile at $t = 0$ s. However, we must make assumptions in order to initialize the density profiles of the ion species. We use the relative fraction x_i of each ion i at each altitude h given by the Viking I measurements [e.g., *Hanson et al.*, 1977]. We note that these measurements are the only ion density profiles from Mars available at present [e.g., *Nagy et al.*, 2004] until the arrival of the Mars Atmospheric and Volatile Evolution (MAVEN) spacecraft, which will begin providing data in November 2014 [*Folta*, 2010]. Namely, we obtain $x_i(h)$ from the density plots from the work of *Fox* [1993].

$$x_i(h) = \frac{n_i(h)}{\sum_i n_i(h)} \quad \text{with} \quad i = O_2^+, CO_2^+, O^+ \quad (3)$$

Finally, the profiles of Figure 1a are obtained using equations (2) and (3) and the assumption of neutrality of the Martian ionosphere ($\sum_i n_i(h) = n_e(h)$):

$$n_i(h) = x_i(h) n_e(h) \quad (4)$$

At this point, it should be noted that Viking density profiles are limited to a range of altitude between 100 and 300 km. Approximate values of the ion densities above 300 km are obtained by fitting *Chapman*'s [1931] functions to the Viking data profiles in the available altitude ranges. These approximations work particularly well in our region of interest. Consequently, we maintain a high level of confidence in our simulation results in the 100–300 km altitude range. The resulting ion profiles are reproduced in Figure 1a.

[10] The initial values of electron and ion pressures p_e, $p_{O_2^+}$, $p_{CO_2^+}$, and p_{O^+} are shown in Figure 1d. They are calculated using the ideal gas law: $p_\alpha = n_\alpha k_B T_\alpha$, where n_α is the ion or electron density shown in Figure 1a and T_α is the temperature of the species α, with the temperature profiles given in Figure 1c. We assume that all ions have the same initial temperature ($T_i = T_{O_2^+} = T_{CO_2^+} = T_{O^+}$).

[11] The only direct measurements of the ion velocities on Mars are supersonic and super-Alfvénic (∼5 km/s). However, they have been taken transterminator and at high altitude (≳300 km) [*Fränz et al.*, 2010], and no such measurements are available at the altitude of the dynamo region. Consequently, the choices of the initial values of $\vec{V}_{O_2^+}$, $\vec{V}_{CO_2^+}$, and $\vec{V}_{O^+}$ remain somewhat arbitrary. If the ions are created from the neutrals, then it is reasonable to assume that their bulk velocity is of the same order of magnitude as the neutral wind speed and are necessarily subsonic. Therefore, we adopt $|\vec{V}_i| = |\vec{V}_n|$ for all the simulation runs presented in this paper. Equations (6) and (13) show that the collision terms are functions of the vector difference between the ion and neutral velocities. From this, it follows that choosing $\vec{V}_i \perp \vec{V}_n$ at $t = 0$ is the best choice to maximize the effect of the collisional interactions in Mars' ionosphere and to demonstrate how they can produce the dynamo current.

[12] The neutral wind velocity and initial magnetic field are treated as input parameters by the model. We assume a zonal neutral wind with speed equal to 100 m/s along the x-direction (thus, $\vec{V}_i(t = 0)$ is along the y-axis). This value is in reasonable agreement with the typical values quoted by *Leovy* [2001] for wind at jet stream altitude, and the results of Mars Global Circulation models [e.g., *Forget et al.*, 1999; *Bougher et al.*, 2008]. For the sake of simplicity, we assume uniform initial wind velocity throughout the simulation domain.

[13] Finally, the planetary magnetic field is assumed to be radial (such fields have been reported away from the magnetic anomaly and on the nightside in, e.g., *Mitchell et al.* [2001], *Brain et al.* [2005], and *Ferguson et al.* [2005]. Magnitudes about 20 nT are expected in multiple locations and are consistent with observations [e.g., *Vignes et al.*, 2000], while 2000 nT are expected to be exceptional and much more localized. Indeed, this latter case is more similar to the maximum radial fields of magnitude ∼1500 nT recorded below 200 km by MGS and reported in *Mitchell et al.* [2001, Plate 1]. We note that a 2000 nT field is found as a local value below 100 km [*Acuña et al.*, 1999] but is a very useful theoretical configuration for the validation of our model. Although highly idealized, this model magnetic field is sufficient to demonstrate the development of currents in Mars' dynamo region.

2.2. Multifluid Magnetohydrodynamic Model

[14] The specificities of Mars' ionosphere discussed above led us to develop a multifluid model of the ionosphere (following the same base principles as *Paty and Winglee*'s [2006] model of Ganymede's atmosphere). For each ion species i ($i = O_2^+$, CO_2^+, O^+), the model uses the continuity equation (5), the momentum equation (6), and the equation of state (7) to derive the ion number density n_i, velocity $\vec{V}_i$, and pressure P_i.

$$\frac{\partial \rho_i}{\partial t} = -\nabla \cdot \left(\rho_i \vec{V}_i\right) \tag{5}$$

$$\rho_i \frac{\partial \vec{V}_i}{\partial t} = -\rho_i \left(\vec{V}_i \cdot \nabla\right) \vec{V}_i + e n_i \left(\vec{E} + \vec{V}_i \times \vec{B}\right) - \nabla P_i + \frac{\rho_i \vec{g}_M}{\left(1 + \frac{z}{R_M}\right)^2} + \sum_{\beta \neq i} \rho_i \nu_{i-\beta} \left(\vec{V}_\beta - \vec{V}_i\right) \tag{6}$$

$$\frac{\partial P_i}{\partial t} = -\gamma_i \nabla \cdot \left(P_i \vec{V}_i\right) + (\gamma_i - 1) \left(\vec{V}_i \cdot \nabla\right) P_i \tag{7}$$

It should be noted that equation (5) assumes equality of source and loss terms. This corresponds to a situation of a dayside atmosphere at chemical equilibrium, where photoionozation balances electron attachment.

[15] The electron number density n_e, velocity $\vec{V}_e$, and pressure P_e are calculated using the plasma approximation (8), the definition of the plasma conduction current (9), and the equation of state for electrons (10).

$$n_e = \sum_i n_i \tag{8}$$

$$\vec{V}_e = \sum_i \frac{n_i \vec{V}_i}{n_e} - \frac{\vec{J}}{e n_e} \tag{9}$$

$$\frac{\partial P_e}{\partial t} = -\gamma_e \nabla \cdot \left(P_e \vec{V}_e\right) + (\gamma_e - 1) \left(\vec{V}_e \cdot \nabla\right) P_e \tag{10}$$

Finally, the conduction current $\vec{J}$, the magnetic field $\vec{B}$, and the electric field $\vec{E}$ are obtained using Maxwell-Faraday's equation (12), Maxwell-Ampère's law (where the displacement current is considered negligible, due to slow charge motions) (11), and the generalized Ohm's law (13), respectively. It should be noted that (13) is obtained from the momentum equation for electrons, where the time derivative of the electron momentum is neglected, due to the small mass of the electron.

$$\vec{J} = \frac{\nabla \times \vec{B}}{\mu_0} \tag{11}$$

$$\frac{\partial \vec{B}}{\partial t} = -\nabla \times \vec{E} \tag{12}$$

$$\vec{E} = -\vec{V}_e \times \vec{B} - \frac{\nabla P_e}{e n_e} + \frac{m_e}{e} \sum_{\beta \neq e} \nu_{e-\beta} \left(\vec{V}_\beta - \vec{V}_e\right) \tag{13}$$

The constants μ_0, γ_α, e, and k_B are defined in Table 2.

[16] The atmospheric conductivity and resistivity effects are directly reflected through the momentum transfer collision terms in equations (6) and (13). The elastic collision terms between two particles α and β are expressed as $\rho_\alpha \nu_{\alpha-\beta} \left(\vec{V}_\beta - \vec{V}_\alpha\right)$. We recall that the collision frequency $\nu_{\alpha-\beta}$ is proportional to the density of target β: $\nu_{\alpha-\beta} \propto n_\beta$ [e.g., *Schunk and Nagy*, 2000, p. 88, equation (4.117)]. Besides, Figure 1 shows that $n_{CO_2,O} \gg n_{O_2^+,CO_2^+,O^+,e}$; therefore, neutrals are the preferred targets in elastic collisions with the projectiles (ions in the momentum equation (6), electron in the generalized Ohm's law (13)). Ultimately, the system of equations that we solve includes all the collision frequencies listed in Table 1 and excludes nonelastic collisions at the present stage of development of the model.

Table 2. Definitions of the Constants Used in the Model

Symbol	Definition	Value
μ_0	Free space permeability	
k_B	Boltzmann constant	
e	Elementary charge	
c	Speed of light in free space	
$\gamma_{O_2^+}$	O_2^+ specific heat ratio	1.40
$\gamma_{CO_2^+}$	CO_2^+ specific heat ratio	1.28
γ_{O^+}	O^+ specific heat ratio	1.66
γ_e	Electron specific heat ratio	1.66

2.3. Methods

[17] The system of equations (5)–(13) is discretized using a centered difference scheme [e.g., *LeVeque*, 2007, p. 8] with the following uniform mesh widths: $\delta x = 10$ km, $\delta y = 10$ km, and $\delta z = 3$ km. In order to solve the system using a second-order, two-stage Runge-Kutta method [e.g., *LeVeque*, 2007, p. 124], the time step δt is recalculated after each iteration to satisfy the Courant-Friedrich-Lewy conditions [*Courant et al*., 1928]. For a magnetohydrodynamic flow, the Courant-Friedrich-Lewy conditions must be satisfied for both the hydrodynamical flows of ions and electrons, and the magnetic speeds (specifically, the Alfvén and fast magnetosonic wave velocities).

[18] We assume that the individual species can be treated separately for the sake of the determination of a Courant-Friedrich-Lewy criterion. For each ion i, we define the Alfvén, sonic, and fast magnetosonic wave speeds denoted V_A^i, V_s^i, and V_{fast}^i, respectively [e.g., *Chen*, 1984, p. 145]:

$$V_A^i = \sqrt{\frac{B^2}{\mu_0 m_i n_i}} \tag{14}$$

$$V_s^i = \sqrt{\frac{\gamma_e p_e + \gamma_i p_i}{m_i n_i}} \tag{15}$$

$$V_{fast}^i = c \sqrt{\frac{V_s^{i\,2} + V_A^{i\,2}}{c^2 + V_A^{i\,2}}} \tag{16}$$

Then, we define critical time steps δt_{cr}^i for each ion i:

$$\delta t_{cr}^i = \min \left(\frac{\delta x}{\max\left(|V_x^i| + |V_{fast}^i|\right)}, \frac{\delta y}{\max\left(|V_y^i| + |V_{fast}^i|\right)}, \frac{\delta z}{\max\left(|V_z^i| + |V_{fast}^i|\right)} \right) \tag{17}$$

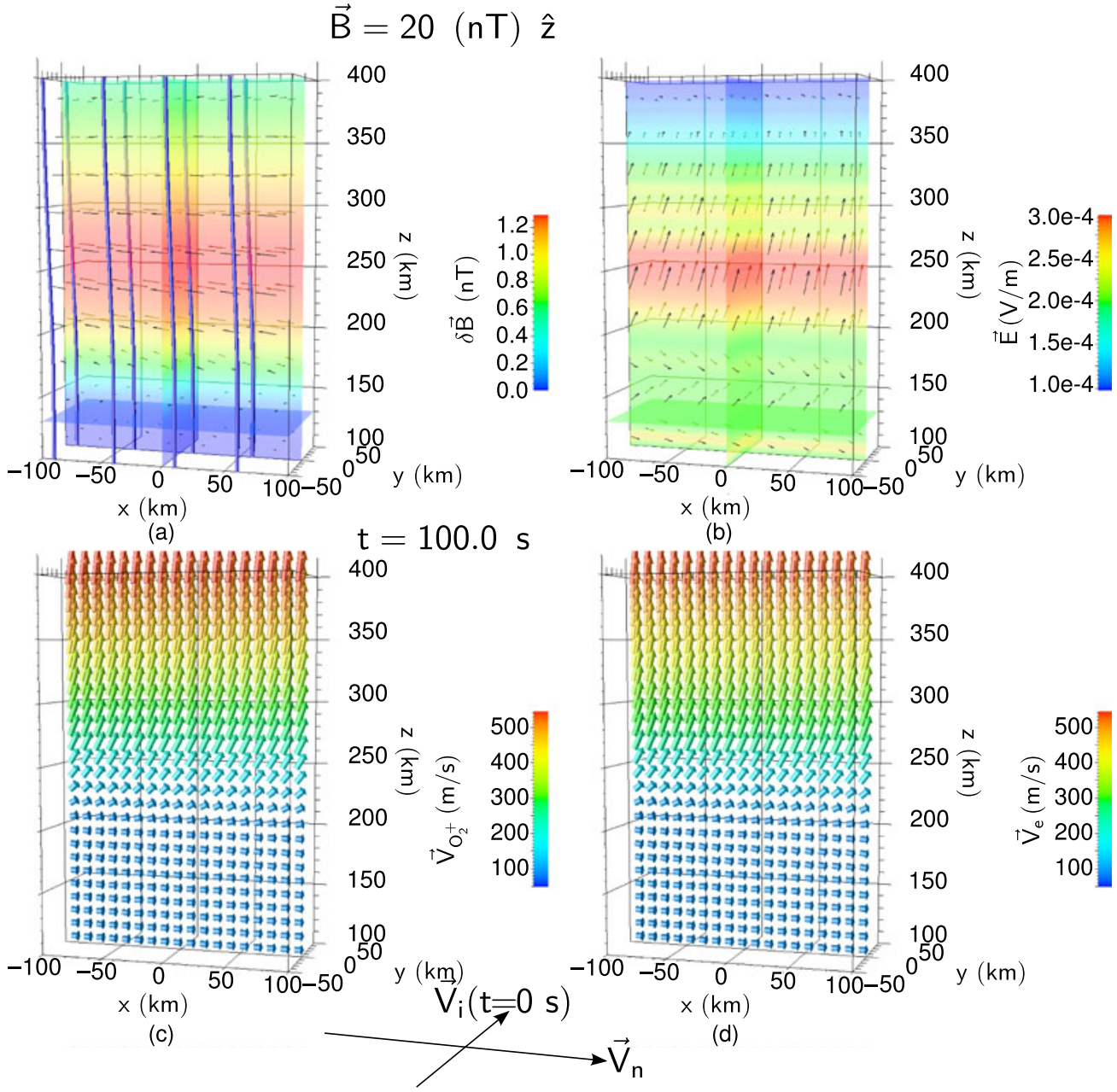

Figure 3. Simulation results at t = 100.0 s for an initial magnetic field $\vec{B}$ = 20 nT $\hat{z}$. (a) Magnetic field perturbation $\delta\vec{B} = \vec{B}(t) - \vec{B}(0)$ displayed in the planes x = 0 km, y = 0 km, and z = 130 km. The solid blue lines show the geometry of the magnetic field lines. (b) Electric field displayed in the same way as Figure 3a. (c and d) O_2^+ and electron velocities in the vertical plane y = 0 km. Figures 3a and 3b use solid black arrows to display the direction of $\delta\vec{B}$ and $\vec{E}$, respectively. On the other hand, Figures 3c and 3d use colored arrows to display the direction and speed of the fluid flows of O_2^+ ions and electrons in the central vertical plane at y = 0 km. The speeds of the flows are shown by both the length of the arrows and the colormap. High velocities use longer arrows and yellow-red colors, while low velocities use shorter arrows and blue-green colors. Finally, the directions of the neutral wind and of the charge carriers' initial velocity are represented using black arrows marked $\vec{V}_n$ and $\vec{V}_i$, respectively.

We choose the conservative value for δt_{CFL} given below:

$$\delta t_{\mathrm{CFL}} = \min_i \left(\delta t_{\mathrm{cr}}^i\right) \tag{18}$$

and finally, we update the time step after each iteration as follows:

$$\delta t = C\,\delta t_{\mathrm{CFL}} \quad \text{with } C = 0.1 \tag{19}$$

[19] Typically, according to (19), δt remains such that $\delta t \lesssim 1$ ms throughout the simulation run. Such small time steps require high performance computing, and consequently, the solver is parallelized using the MPI library [e.g., *Pacheco*, 1996] using the Portable, Extensible Toolkit for Scientific computation [*Balay et al.*, 1997, 2011a, 2011b]

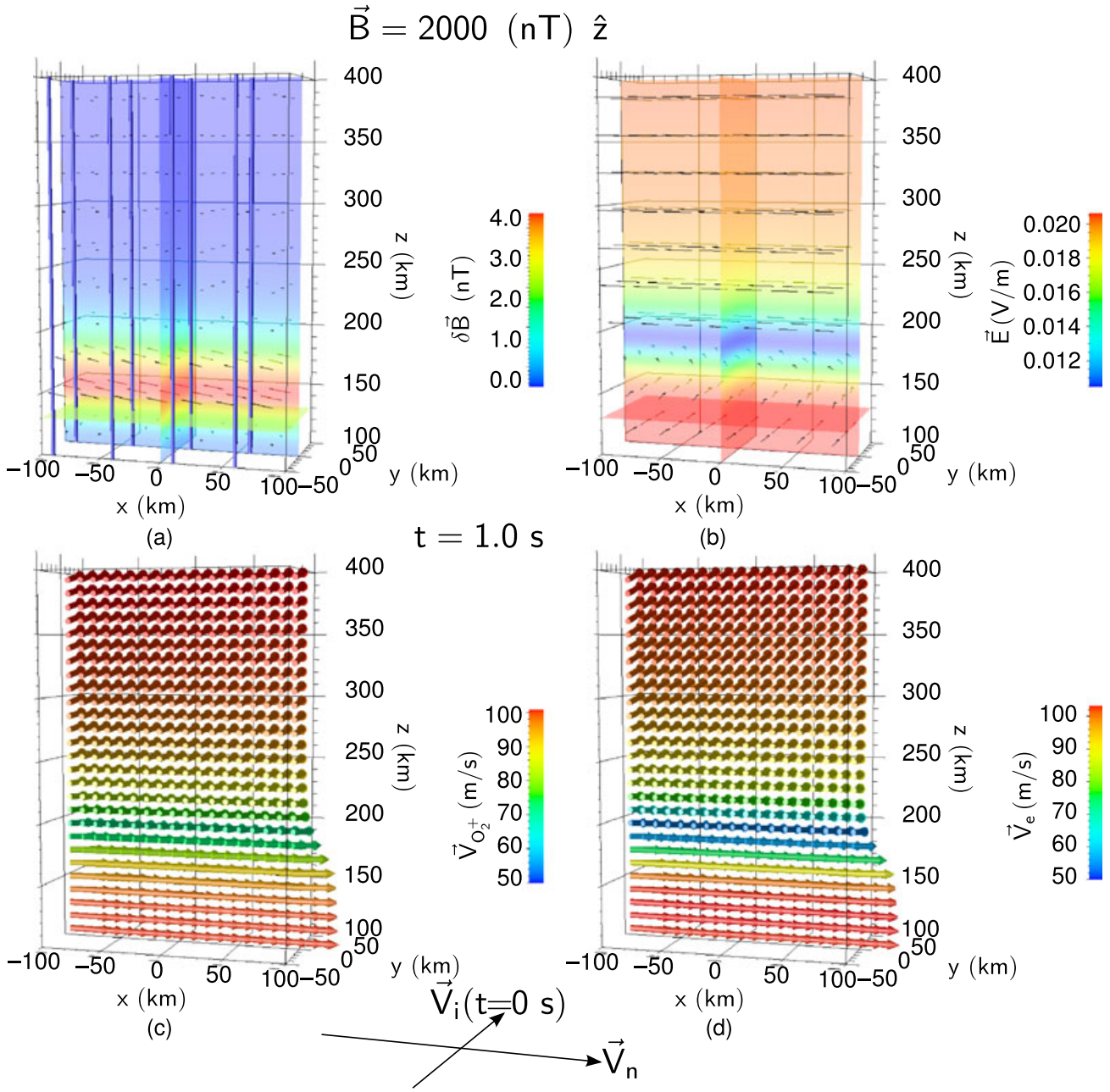

Figure 4. Simulation results at t = 1.0 s for an initial magnetic field $\vec{B}$ = 2000 nT $\hat{z}$. (a, b, c, and d) Same as in Figure 3.

and runs on the Georgia Institute of Technology Atlas-6 cluster.

[20] We choose a domain widely enclosing the phenomenon, so that relatively simple boundary conditions can be used without significantly affecting the processes occurring in the region of interest. We use simple Neumann boundary conditions for all variables.

$$\frac{\partial f}{\partial \hat{n}} = 0 \quad \text{with } f = \vec{V}_i, n_i, p_i, p_e, \vec{B} \tag{20}$$

where $\hat{n}$ is the vector normal to the boundary. Precisely, the value of a variable in a boundary cell is carried from the nearest cell along the direction $-\hat{n}$, effectively leading to null flux boundary conditions conforming to equation (20).

[21] We apply the same Neumann boundary conditions for $f = n_e$, $\vec{V}_e$, $\vec{E}$, $\vec{J}$. We note that this is partially redundant with equations (8), (9), (11), and (13). Yet the presence of spatial derivatives in Ampère's and Ohm's laws makes it impractical to explicitly calculate the boundary values of $\vec{J}$ and $\vec{E}$ (and subsequently of $\vec{V}_e$) based on equations (11) and (13).

[22] Setting the upper boundary condition raises the issue of Mars' atmospheric escape. Though a particularly interesting problem, it falls beyond the scope of this work. Here we focus on effects located in the dynamo region, which ranges from 100 to 250 km altitude. We tested various boundary conditions (e.g., $\frac{\partial^2 f}{\partial \hat{n}^2} = 0$) and noticed no significant differences. In the present formulation of the model, the use

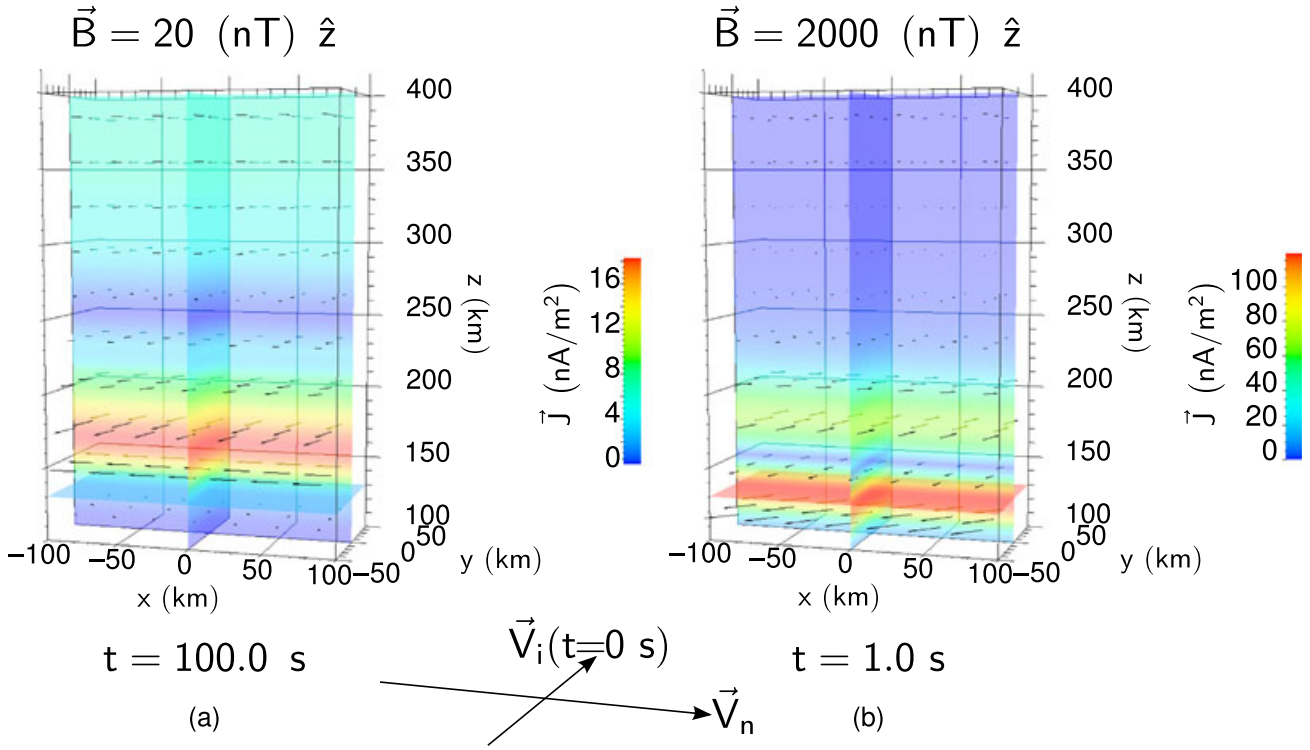

Figure 5. Current density (a) at t = 100.0 s for an initial magnetic field $\vec{B}$ = 20 nT $\hat{z}$ and (b) at t = 1.0 s for an initial magnetic field $\vec{B}$ = 2000 nT $\hat{z}$. The magnitude of the current density is displayed in three planes: x = 0 km, y = 0 km, and z = 130 km, and the black arrows represent directions of the current sampled throughout the domain.

of Neumann boundary conditions (20) and the absence of sources/sink in the continuity equations (5) means that a "true" steady state cannot be reached, due to outflows of the initial quantities through the boundaries. However, despite these outflows, we calculate a relative loss of charge carriers in the entire simulated domain $\lesssim$3% at the time of the snapshots of Figures 3 to 6. In addition, it should be noted that the upper boundary is far enough from the region of interest, so that it has very limited influence on the dynamics in the dynamo region. Consequently, it appears that the simple Neumann conditions employed here represent a satisfactory treatment of the boundaries of our simulation domain.

[23] The results from two test case scenarios are presented in sections 3 and 4. All other parameters remaining the same, the magnetic field amplitude is varied from 20 to 2000 nT, in order to demonstrate its effects on the dynamo currents.

3. Results

[24] In this section, we report results from two representative simulation runs with $\vec{B}$= 20 nT $\hat{z}$ and $\vec{B}$= 2000 nT $\hat{z}$, hereafter referred to as "Case 1" and "Case 2," respectively. Our results demonstrate the formation of a dynamo current in the altitude range predicted by the calculations that produced Figure 2.

[25] Figures 3 and 4 show representative still frames for case 1 after 100.0 s, and for case 2 at t = 1.0 s, respectively. The simulations performed in the framework of this paper demonstrate the buildup of electrical currents that generates a perturbation of the magnetic field, which ultimately results in the formation of Alfvén waves. These waves propagate at the Alfvén speed $\vec{V}_A$ from equation (14).

[26] For the case of a uniform vertical magnetic field, Alfvén waves accelerate as they propagate upward toward regions where ions are scarce. Although it is a useful approximation, the hypothesis of a strong magnetic field near z = 400 km most likely leads to overestimated field values near the upper boundary. The fields at this location are additionally increased by the reflection on the top of the simulation domain. It is therefore necessary to choose a time of observation prior the Alfvén wave reflection at that boundary [*Vasyliūnas*, 2012], i.e., at a time when the simulation runs are still unperturbed by these numerical artifacts. Each figure displays the magnitudes and directions of magnetic field perturbation $\delta\vec{B}$, the electric field $\vec{E}$, and velocities of the dominant ion O_2^+ and electrons ($\vec{V}_{O_2^+}$ and $\vec{V}_e$) in Figures 3a, 3b, 3c, and 3d, respectively. Figures 3a and 3b use surface maps at x = 0 km, y = 0 km, and z = 130 km to show the magnitudes of $\delta\vec{B}$ and $\vec{E}$ throughout simulation domain. In addition, the solid blue lines in Figure 3a show the shape of the magnetic field lines at the time of the snapshot (100.0 s for case 1 and 1.0 s for case 2) and emphasize their distortion at the altitude of the dynamo region under the influence of the magnetic perturbation.

[27] The choice of a uniform velocity for the charge carriers at t = 0 s, of a uniform neutral wind, and of a uniform initial magnetic field $\vec{B} = B_0\hat{z}$ limits horizontal variations. Consequently, the physical processes of interest vary along the z-direction only. The observation of the dynamic evolution of Figure 3a shows a perturbation of the magnetic field

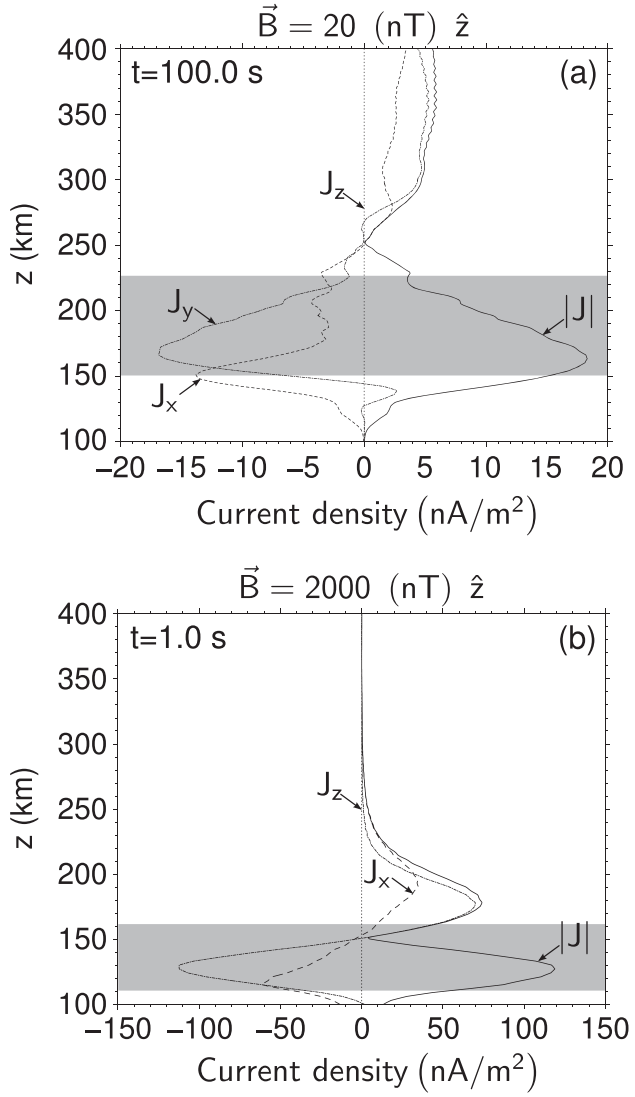

Figure 6. Current density components at the center of the simulation domain. The snapshot is taken (a) at t = 100.0 s for an initial magnetic field $\vec{B}$ = 20 nT $\hat{z}$ and (b) at t = 1.0 s for an initial magnetic field $\vec{B}$=2000 nT $\hat{z}$. The gray shading emphasizes the location of the dynamo region expected from Figure 2.

$\delta B \approx$ 1–2 nT, i.e., about 5–10% of the crustal field. The perturbation is created between 175 and 200 km altitude, dividing the local atmosphere into three regions: (1) a low altitude region where collisional interactions guide both ion and electron trajectories; (2) a high altitude region where all charged particles are magnetized and follow a gyromotion; and (3) the dynamo region in-between, where electrons are magnetized but ions are not. It is then moved upward by pressure gradients and hydrodynamic effects. In addition, it can be noticed that in the lower region of the atmosphere, the electric field possesses a strong component along $\hat{y}$ and $E_x \approx 0$, while at higher altitudes, $\vec{E}$ is predominantly directed toward the negative $\hat{x}$ direction. The observation of Figure 3, and specifically of the ion and electron velocities (Figures 3c and 3d), reveal that below ∼200–225 km, both species move along the direction of the neutral wind at ∼100 m/s. Above, hydrodynamic processes favor an upward vertical flow at even higher speed.

[28] Figure 4 is the same as Figure 3 but for an initial magnetic field $\vec{B}$ = 2000 nT $\hat{z}$. Figure 4a shows a perturbation in $\vec{B}$ migrating upward that is about 3 times greater than the perturbation of Figure 3a, but smaller relative to the magnitude of the crustal field. Figure 4b appears to be simpler than its counterpart in Figure 3, suggesting that one process may overcome all others in several regions of the atmosphere in this case. In particular, it is clear that in the lower, denser part of the atmosphere, the electric field is directed toward $+\hat{y}$, while in the upper, less dense part of the domain, $\vec{E}$ is essentially directed along the negative $\hat{x}$ direction. Figures 4c and 4d show similar behavior of ion and electron velocities. At higher altitudes, the ion and electron flows remain mostly undisturbed and move with their original speed. The flow progressively turns toward the $+\hat{x}$ direction at lower altitude and essentially moves with the neutral wind below $z \approx$150 km. An interesting difference with Figure 3 is that the particle velocities seem mostly confined in the horizontal planes (x-y planes). This difference can be explained by the choice of the snapshot time, which is dictated by hydrodynamic and electrodynamic timescales (see discussion in section 4).

[29] Both panels of Figure 5 use the formatting of Figures 3a, 3b, 4a, and 4b to compare the formation of dynamo currents in case 1 (Figure 5a) and case 2 (Figure 5b). Figures 5a and 5b allow us to clearly identify a region with the strongest conduction currents. The region is located between ∼125 and ∼250 km in case 1, and between 110 km and 140 km in case 2. Figure 2 suggests a dynamo region spanning from approximately 150 to 225 km altitude for a 20 nT applied field, and from $z \approx$110 km to $z \approx$160 km for a 2000 nT strong magnetic field. In both cases 1 and 2, the currents in these regions follow roughly the same direction but differ by a factor of 5 approximately, with maximum current densities being about 15–20 nA/m^2 for case 1 and 125 nA/m^2 for case 2.

[30] The above results are confirmed by Figure 6. Figure 6 displays the individual components (J_x, J_y, and J_z) and the norm ($|J|$) of the electric current on a vertical scan in the center of the simulation domain (at x = 0, y = 0). Figures 6a and 6b correspond to cases 1 and 2, respectively, and further complements the conclusions drawn from Figure 5.

[31] In the next section, we discuss the above results and provide context and explanation of the development of dynamo currents in Mars' ionosphere depending on the magnitude of the crustal fields.

4. Discussion

[32] The simulations entitled case 1 and case 2 have been performed with the same initial conditions provided by or derived from Figure 1. In both cases, the initial velocities of all charge carriers is chosen to be 100 m/s along the y-axis, i.e., normal to both the vertical magnetic field $\vec{B}$ and to the neutral wind $\vec{V}_n$ = 100 m/s $\hat{x}$, to maximize the effect of the Lorentz forces on the plasma (see section 2).

[33] Throughout this paper, we adopted uniform initial vertical geometries for the magnetic fields. This obviously does not reproduce the complexity of the Martian magnetic

topology as evidenced by, e.g., the percent reconnection at 400 km of magnetic field lines to the interplanetary magnetic field (IMF) [*Brain et al.*, 2007]. Yet their simplicity is a valuable asset for the purpose of understanding the physics of the formation of the dynamo current, the interactions between the lower ionosphere and the crustal fields, and for the validation of a new model. A 20 nT magnetic field corresponds to a typical weak-to-moderate crustal field as measured by Mars Global Surveyor Magnetometer [*Acuña et al.*, 2001; *Brain et al.*, 2003]. The choice of a 2000 nT field may overestimate the maximum field found on the surface but presents the advantage of creating a theoretical dynamo region quite distinct from the one created by a 20 nT magnetic field (see Figure 2). It is possible to obtain a theoretical dynamo region above ∼250 km. This would be achieved by decreasing the magnitude of the magnetic field ($B \ll 1$ nT), but such low fields are hardly able to create noticeable perturbation in the dynamics of the charge carriers. In addition, fields with extremely low magnitudes are unlikely, insofar as the piled up solar wind on the dayside at 250 km is at least 20 nT, and the magnetotail field on the nightside is at least 5 nT. On the other hand, increasing the magnetic field above 2000 nT would not only become very unrealistic but would also lower the dynamo region into a region where the charge carriers are scarce. Indeed, both measurements of the electron number density (see [e.g., *Kliore*, 1992] for Viking I and [e.g., *Bougher et al.*, 2001] for MGS) and models derived from *Chapman*'s [1931] theory for dayside ionospheric profiles [e.g., *Pi et al.*, 2008] show a dramatic decrease in the electron number density below $z \approx 100$ km. In the absence of charge carriers, no dynamo region can develop, and the existence of a dynamo region below altitude 50–100 km is unlikely under nominal conditions such as those presented in Figure 1 and adopted for the simulations developed in this paper. A 2000 nT magnitude maximizes the effect of collisions between the charge carriers and the neutral particles CO_2 and O, via the placement of the dynamo region near the peak of the charged species densities (see Figures 1 and 2b). This result is consistent with *Lillis et al.*'s [2011] estimated altitude of the dynamo region for local dipolar fields with similar intensity. In particular, *Lillis et al.*'s [2011] Figure 9 also suggests that in that situation, the dynamo region develops near the maximum in electron density.

[34] Figures 5 and 6 emphasize the formation of a dynamo current between 150 and 225 km for a 20 nT applied field and between 110 and 150 km for a 2000 nT magnetic field, i.e., at the location of the dynamo regions predicted by Figure 2. For two uncoupled flows of ions and electrons, the maximum electrical current is obtained when the positive and negative fluids move in opposite directions (namely, $\vec{V}_e = -\vec{V}_i$). It can be safely assumed that after the transitory stage, all ions in the dynamo region are moving due to their collisions with the neutrals, effectively being entrained by the neutral wind and moving at the speed $\vec{V}_i = \vec{V}_n$. For singly charged ions, under the plasma approximation, the maximum current in the dynamo region for such uncoupled flows is $J_{max} \approx 2en_eV_n$. Given the values of n_e and $\vec{V}_n$ for cases 1 and 2 ($n_e|_{z=175\text{ km}} \approx 10^4$ cm^{-3}, $n_e|_{z=120\text{ km}} \approx 10^5$ cm^{-3}, and V_n=100 m/s), we calculate $J_{max} \approx 10^{-7}$ and 10^{-6} A/m^2 for cases 1 and 2, respectively. The modeled

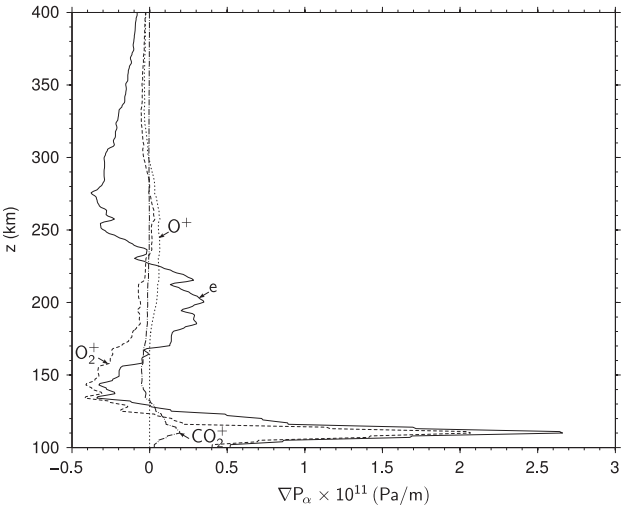

Figure 7. Pressure gradients of O_2^+, CO_2^+, and O^+, and electrons at $t = 0$ s, $x = 0$ km, and $y = 0$ km, based on the pressure estimates provided in Figure 1d.

dynamo current densities are naturally expected to be below the analytically calculated maximum currents. Evidence of the coupling between the flows of positive and negative charge carriers is found in Figures 3c, 3d, 4c, and 4d, as ions and electrons clearly do not move in opposite directions. Coincidently, Figures 5 and 6 suggest that the actual maximum values of the dynamo currents are about an order of magnitude less than the "back-of-the-envelope calculations" above. Yet it is important to notice that the factor of 10 difference between the currents in cases 1 and 2 estimated from the analytical calculations is accurately reproduced by the model. The dependencies on n_e and V_n have been confirmed by performing simulations (not presented here for the sake of brevity) in which the neutral wind speed is varied with all other parameters remaining the same. Using an electron transport model, *Fillingim et al.* [2010] calculated Mars' atmospheric current between 100 and 300 km altitudes. In this work, the currents range from 10^{-1} to 10^3 nA/m^2, fully consistent with the simulation results presented in this paper. In another back-of-the-envelope estimate, *Withers et al.* [2005] suggested currents of 30 A/km over a 10 km thick region for a 100 nT field, which is equivalent to a current density of 3.0×10^{-6} A/m^2, consistent with the results of the current project. In a more detailed calculation, *Withers* [2008] found current densities of 10^{-8} A/m^2 for a 50 nT field, which is noticeably smaller than our results.

[35] Both panels of Figure 6 indicate the existence of a second region of currents above the dynamo region. *Fillingim et al.* [2010] attributed similar currents to the interaction of pressure gradients with the magnetic field. Figure 7 displays the pressure gradients of each species at $t = 0$ s, using a central difference scheme applied to the profiles of Figure 1d. Based on this plot, pressure gradients are expected to both contribute to current densities in the dynamo region and support the development of currents in other part of the ionosphere as shown in Figure 6.

[36] Figure 2 shows that collisions play little, if any, role at high altitudes. At these locations, the ion flow remains relatively unperturbed except by the hydrodynamic effects,

which provide the ions and electrons with a vertical motion. It should be noted that these effects appear due to the initial temperature and density profiles that are used in the model.

[37] The simulation results presented in Figure 3c show that particles are moving with their initial velocity in the horizontal plane (normal to $\vec{B}$) for $z \gtrsim 350$ km, creating an induced electric field $-\vec{V}_e(t = 0) \times \vec{B} = -2 \times 10^{-6}$ V/m $\hat{x}$, which is confirmed by Figure 3b. On the other hand, collisions are the driving engine of motions of charged species in higher neutral density regions, i.e., at lower altitudes. Consequently, all species move in a relatively uniform flow with the velocity $\vec{V}_n$ for $z \lesssim 120$ km. The theoretical induced electric field at this altitude is therefore $-\vec{V}_n \times \vec{B} = +2 \times 10^{-6}$ V/m $\hat{y}$, consistent with the model results shown in Figure 3b.

[38] The results of Figure 4 further support the above discussion. Indeed, when the initial magnetic field is increased by 2 orders of magnitude, the term $-\vec{V}_e \times \vec{B}$ in equation (13) becomes even more dominant, and we find that the modeled electric field is indeed almost equal to the predicted theoretical field. The main difference between the charged species flows in cases 1 and 2 is the absence of a vertical component to the velocities in the latter. The explanation lies in the respective timescales of hydrodynamic and electromagnetic effects. The timescale of electromagnetic effects τ_{EM} can be estimated based on the time it takes to travel through the full height of the domain at the Alfvén speed V_A (given by equation (14)):

$$\tau_{EM} = \frac{L_z}{V_A} \tag{21}$$

Using equations (14) and (21), it naturally follows that τ_{EM} is inversely proportional to the applied magnetic field. Therefore, the snapshots of cases 1 and 2 are taken at the same "electromagnetic time" t/τ_{EM}, insofar at case 1 is observed 100 times later than case 2, but employs a 100 times smaller magnetic field.

[39] On the other hand, a change in $\vec{B}$ does not affect the timescale of the hydrodynamic effects, and therefore, at the time of the snapshot of Figure 3, hydrodynamic processes have seemingly affected the simulation. Conversely, the hydrodynamic effects have yet to modify the flow in case 2 after $t = 1.0$ s, and a substantial vertical component is indeed present later on in the run. It should be noted that the study of the evolution of the maximum current density with time confirms that the system has stabilized at the times chosen for cases 1 and 2.

[40] The above results demonstrate that the dynamo currents are directly impacted by the speed of the neutral wind in the collisional regions and in particular in the dynamo region. They are also indirectly influenced by the strength of the local magnetic field, insofar as the magnitude of $\vec{B}$ defines the location of the dynamo region, and therefore the densities of neutrals and charged species in the region where the current develops. In contrast, the electric field mostly depends on the Lorentz force applied to electrons, and this dependence increases with the strength of the applied magnetic field. Consequently, the electric field depends directly on the magnetic field and on the electron velocity, which is greatly correlated to the neutral wind in the highly collisional regions.

[41] From the above discussion, the model displays very promising features as a complementary tool to future missions to Mars. In particular, it will benefit from the measurements from Mars Atmospheric and Volatile Evolution (MAVEN) mission, scheduled for launch in late 2013 [*Folta*, 2010]. This mission will focus on Mars' upper atmosphere and provide densities and temperatures of electrons, ions, and neutrals (both with composition information), as well as solar EUV and precipitating electrons, which are particularly appropriate for the improvement of the initial conditions and parameters used in the model presented in this paper.

5. Conclusions

[42] In this work, we introduced a new model of Mars' particle charged atmosphere. Mars' atmospheric electrodynamics is made more intricate, in part by the complex topology of the magnetic field, but also due to the nonhomogeneous nature of Mars' atmosphere and ionosphere. The model is three-dimensional, dynamic, self-consistent, and multifluid. Multifluid models are known to be complex due to their profoundly coupled nature but are also necessary to study the mechanisms driving the dynamics of planetary atmospheres [*Vasyliūnas*, 2012], and particularly in the formation of a dynamo region. The results presented in this paper have proven to be remarkably robust and confirm the existence of a conduction current in the expected dynamo region of Mars' atmosphere. The location and shape, as well as the magnitude of the dynamo currents depend on the local geometry and strength of the magnetic field. This paper supports the study of various complex magnetic geometries (J. A. Riousset, in preparation, 2013). Our results show consistency with analytical predictions in terms of location and magnitude of the dynamo currents but also suggest a reasonable explanation for the direction and magnitude of the electric field in various parts of the simulation domain, both qualitatively and quantitatively. Overall, this work constitutes a solid basis toward an improved understanding of the electrodynamics of Mars' atmosphere and may ultimately pose potential considerations for the interpretation of MAVEN data.

[43] **Acknowledgments.** The authors gratefully acknowledge the anonymous reviewers for their valuable feedback on the manuscript. This work was supported by the National Aeronautics and Space Administration (NASA) under grant NNX10AM88G-MFRP to the Georgia Institute of Technology.

[44] Masaki Fujimoto thanks the reviewers for their assistance in evaluating this paper.

References

Acuña, M. H., et al. (1999), Global distribution of crustal magnetization discovered by the Mars Global Surveyor MAG/ER experiment, *Science*, *284*, 790, doi:10.1126/science.284.5415.790.

Acuña, M. H., et al. (2001), Magnetic field of Mars: Summary of results from the aerobraking and mapping orbits, *J. Geophys. Res.*, *106*, 23,403–23,418, doi:10.1029/2000JE001404.

Arkani-Hamed, J. (2004), A coherent model of the crustal magnetic field of Mars, *J. Geophys. Res.*, *109*, E09005, doi:10.1029/2004JE002265.

Balay, S., W. D. Gropp, L. C. McInnes, and B. F. Smith (1997), Efficient management of parallelism in object oriented numerical software libraries, in *Modern Software Tools in Scientific Computing*, edited by E. Arge, A. M. Bruaset, and H. P. Langtangen, pp. 163–202, Birkhäuser Press, Boston, Mass.

Balay, S., J. Brown, K. Buschelman, V. Eijkhout, W. D. Gropp, D. Kaushik, M. G. Knepley, L. C. McInnes, B. F. Smith, and H. Zhang, (2011a), PETSc users manual, *Tech. Rep. ANL-95/11 - Revision 3.2*, Argonne National Lab.

Balay, S., J. Brown, K. Buschelman, W. D. Gropp, D. Kaushik, M. G. Knepley, L. C. McInnes, B. F. Smith, and H. Zhang (2011b), PETSc Web page. http://www.mcs.anl.gov/petsc.

Bougher, S. W., S. Engel, D. P. Hinson, and J. M. Forbes (2001), Mars Global Surveyor Radio Science electron density profiles: Neutral atmosphere implications, *Geophys. Res. Lett.*, *28*, 3091–3094, doi:10.1029/2001GL012884.

Bougher, S. W., P.-L. Blelly, M. Combi, J. L. Fox, I. Mueller-Wodarg, A. Ridley, and R. G. Roble (2008), Neutral upper atmosphere and ionosphere modeling, *Space Sci. Rev.*, *139*, 107–141, doi:10.1007/s11214-008-9401-9.

Brain, D. A., F. Bagenal, M. H. Acuña, and J. E. P. Connerney (2003), Martian magnetic morphology: Contributions from the solar wind and crust, *J. Geophys. Res.*, *108*, 1424, doi:10.1029/2002JA009482.

Brain, D. A., J. S. Halekas, R. Lillis, D. L. Mitchell, R. P. Lin, and D. H. Crider (2005), Variability of the altitude of the Martian sheath, *Geophys. Res. Lett.*, *32*, L18203, doi:10.1029/2005GL023126.

Brain, D. A., R. J. Lillis, D. L. Mitchell, J. S. Halekas, and R. P. Lin (2007), Electron pitch angle distributions as indicators of magnetic field topology near Mars, *J. Geophys. Res.*, *112*, A09201, doi:10.1029/2007JA012435.

Brecht, S. H., and S. A. Ledvina (2010), The loss of water from Mars: Numerical results and challenges, *Icarus*, *206*(1), 164–173, doi:10.1016/j.icarus.2009.04.028.

Brecht, S. H., and V. A. Thomas (1988), Multidimensional simulations using hybrid particles codes, *Comput. Phys. Commun.*, *48*, 135–143, doi:10.1016/0010-4655(88)90031-8.

Cain, J. C., B. B. Ferguson, and D. Mozzoni (2003), An n = 90 internal potential function of the Martian crustal magnetic field, *J. Geophys. Res.*, *108*, 5008, doi:10.1029/2000JE001487.

Chapman, S. (1931), The absorption and dissociative or ionizing effect of monochromatic radiation in an atmosphere on a rotating Earth, *Proc. Phys. Soc. London*, *43*, 26–45, doi:10.1088/0959-5309/43/1/305.

Chen, F. F. (1984), *Introduction to Plasma Physics and Controlled Fusion*, pp. 79–154, Plenum Press, New York.

Chen, R. H., T. E. Cravens, and A. F. Nagy (1978), The Martian ionosphere in light of the Viking observations, *J. Geophys. Res.*, *83*(A8), 3871–3876., doi:10.1029/JA083iA08p03871.

Connerney, J. E. P., M. H. Acuña, P. J. Wasilewski, N. F. Ness, H. Rème, C. Mazelle, D. Vignes, R. P. Lin, D. L. Mitchell, and P. A. Cloutier (1999), Magnetic lineations in the ancient crust of Mars, *Science*, *284*, 794, doi:10.1126/science.284.5415.794.

Courant, R., K. Friedrichs, and H. Lewy (1928), Partial differential equations of mathematical physics, *Math. Ann.*, *100*, 32–74.

Ferguson, B. B., J. C. Cain, D. H. Crider, D. A. Brain, and E. M. Harnett (2005), External fields on the nightside of Mars at Mars Global Surveyor mapping altitudes, *Geophys. Res. Lett.*, *32*, L16105, doi:10.1029/2004GL021964.

Fillingim, M., L. Peticolas, R. Lillis, D. Brain, J. Halekas, D. Lummerzheim, and S. Bougher (2010), Localized ionization patches in the nighttime ionosphere of Mars and their electrodynamic consequences, *Icarus*, *206*(1), 112–119, doi:10.1016/j.icarus.2009.03.005.

Folta, D. C. (2010), Mars Atmosphere and Volatile EvolutioN (MAVEN) mission design, in *Spaceflight Mechanics 2010, Parts I-III, Advances in the Astronautical Sciences,* vol. 136, edited by D. Mortari, T. F. Starchville, A. J. Trask, and J. K. Miller, pp. 1401–1415, Univelt Inc., San Diego, CA. 20th AAS/AIAA Space Flight Mechanics Meeting, San Diego, CA, Feb 14–17.

Forget, F., F. Hourdin, R. Fournier, C. Hourdin, O. Talagrand, M. Collins, S. R. Lewis, P. L. Read, and J.-P. Huot (1999), Improved general circulation models of the Martian atmosphere from the surface to above 80 km, *J. Geophys. Res.*, *104*, 24,155–24,176, doi:10.1029/1999JE001025.

Fox, J. (1993), The production and escape of nitrogen-atoms on Mars, *J. Geophys. Res.*, *98* (E2), 3297–3310, workshop on the Martian surface and atmosphere through time, Boulder,CO, September, 23–25, 1991, doi:10.1029/92JE02289.

Fränz, M., E. Dubinin, E. Nielsen, J. Woch, S. Barabash, R. Lundin, and A. Fedorov (2010), Transterminator ion flow in the Martian ionosphere, *Planet. Space Sci.*, *58*, 1442–1454, doi:10.1016/j.pss.2010.06.009.

Hanson, W. B., and G. P. Mantas (1988), Viking electron temperature measurements: Evidence for a magnetic field in the Martian ionosphere, *J. Geophys. Res.*, *93*(A7), 7538–7544, doi:10.1029/JA093iA07p07538.

Hanson, W. B., S. Sanatani, and D. R. Zuccaro (1977), The Martian ionosphere as observed by the Viking retarding potential analyzers, *J. Geophys. Res.*, *82*, 4351–4363, doi:10.1029/JS082i028p04351.

Harnett, E. M. (2009), High-resolution multifluid simulations of flux ropes in the Martian magnetosphere, *J. Geophys Res.*, *114*, A01208, doi:10.1029/2008JA013648.

Harnett, E. M., and R. M. Winglee (2006), Three-dimensional multifluid simulations of ionospheric loss at Mars from nominal solar wind conditions to magnetic cloud events, *J. Geophys Res.*, *111*, A09213, doi:10.1029/2006JA011724.

Jakosky, B. M., and R. J. Phillips (2001), Mars' volatile and climate history, *Nature*, *412*, 237–244.

Kallio, E., and R. Jarvinen (2012), Kinetic effects on ion escape at Mars and Venus: Hybrid modeling studies, *Earth Planets Space*, *64*(2), 157–163, doi:10.5047/eps.2011.08.014.

Kliore, A. J. (1992), Radio occultation observations of the ionospheres of Mars and Venus, in *Venus and Mars: Atmosphere, Ionosphere, and Solar Wind Interactions, Geophys. Monogr. Ser.,* vol. 66, edited by J. G. Luhrnann, M. Tatrallyay, and R. O. Pepin, pp. 265–276, AGU, Washington, D. C. doi:10.1029/GM066p0265.

Ledvina, S. A., Y. J. Ma, and E. Kallio (2008), Modeling and simulating flowing plasmas and related phenomena, *Space Sci. Rev.*, *139*(1-4), 143–189, Workshop on Comparative Aeronomy, ISSI, Bern, CH, Jun 25–29, doi:10.1007/s11214-008-9384-6.

Leovy, C. (2001), Weather and climate on Mars, *Nature*, *412*, 245–249, doi:10.1038/35084192.

LeVeque, R. J. (2007), *Finite Difference Methods for Ordinary and Partial Differential Equations*, pp. 3–12, SIAM, Philadephia, Pa., doi:10.1137/1.9780898717839.

Lewis, S., M. Collins, P. Read, F. Forget, F. Hourdin, R. Fournier, C. Hourdin, O. Talagrand, and J. Huot (1999), A climate database for Mars, *J. Geophys. Res.*, *104*(E10), 24,177–24,194, doi:10.1029/1999JE001024.

Lillis, R. J., H. V. Frey, and M. Manga (2008), Rapid decrease in Martian crustal magnetization in the Noachian era: Implications for the dynamo and climate of early Mars, *Geophys. Res. Lett.*, *35*, L14203, doi:10.1029/2008GL034338.

Lillis, R. J., M. O. Fillingim, L. M. Peticolas, D. A. Brain, R. P. Lin, and S. W. Bougher (2009), Nightside ionosphere of Mars: Modeling the effects of crustal magnetic fields and electron pitch angle distributions on electron impact ionization, *J. Geophys. Res.*, *114*, E11009, doi:10.1029/2009JE003379.

Lillis, R. J., M. O. Fillingim, and D. A. Brain (2011), Three-dimensional structure of the Martian nightside ionosphere: Predicted rates of impact ionization from Mars global surveyor magnetometer and electron reflectometer measurements of precipitating electrons, *J. Geophys. Res.*, *116*, A12317, doi:10.1029/2011JA016982.

Lillis, R. J., D. A. Brain, G. T. Delory, D. L. Mitchell, J. G. Luhmann, and R. P. Lin (2012), Evidence for superthermal secondary electrons produced by SEP ionization in the Martian atmosphere, *J. Geophys. Res.*, *117*, E03004, doi:10.1029/2011JE003932.

Ma, Y.-J., A. F. Nagy, K. C. Hansen, D. L. DeZeeuw, T. I. Gombosi, and K. G. Powell (2002), Three-dimensional multispecies MHD studies of the solar wind interaction with Mars in the presence of crustal fields, *J. Geophys. Res.*, *107*, 1282, doi:10.1029/2002JA009293.

Ma, Y.-J., A. F. Nagy, I. V. Sokolov, and K. C. Hansen (2004), Three-dimensional, multispecies, high spatial resolution MHD studies of the solar wind interaction with Mars, *J. Geophys. Res.*, *109*, A07211, doi:10.1029/2003JA010367.

Mendillo, M., A. Lollo, P. Withers, M. Matta, M. Pätzold, and S. Tellmann (2011), Modeling Mars' ionosphere with constraints from same-day observations by Mars Global Surveyor and Mars Express, *J. Geophys. Res.*, *116*, A11303, doi:10.1029/2011JA016865.

Mitchell, D. L., R. P. Lin, C. Mazelle, H. Rème, P. A. Cloutier, J. E. P. Connerney, M. H. Acuña, and N. F. Ness (2001), Probing Mars' crustal magnetic field and ionosphere with the MGS Electron Reflectometer, *J. Geophys. Res.*, *106*, 23,419–23,428, doi:10.1029/2000JE001435.

Modolo, R., G. M. Chanteur, and E. Dubinin (2012), Dynamic Martian magnetosphere: Transient twist induced by a rotation of the IMF, *Geophys. Res. Lett.*, *39*, L01106, doi:10.1029/2011GL049895.

Nagy, A. F., et al. (2004), The plasma environment of Mars, *Space Sci. Rev.*, *111*, 33–114, doi:10.1023/B:SPAC.0000032718.47512.92.

Pacheco, P. S. (1996), *Parallel Programming with MPI*, pp. 11–40, Morgan Kaufmann Publishers Inc., San Francisco, Calif.

Paty, C., and R. Winglee (2006), The role of ion cyclotron motion at Ganymede: Magnetic field morphology and magnetospheric dynamics, *Geophys. Res. Lett.*, *33*, L10106, doi:10.1029/2005GL025273.

Pi, X., C. D. Edwards, G. A. Hajj, C. Ao, L. J. Romans, J. L. Callas, A. J. Mannucci, S. W. Asmar, and D. S. Kahan, (2008), A Chapman-layers ionospheric model for Mars, *NASA STI/Recon Technical Report N, 8*, 32,557.

Purucker, M., D. Ravat, H. Frey, C. Voorhies, T. Sabaka, and M. Acuña (2000), An altitude-normalized magnetic map of Mars and its interpretation, *Geophys. Res. Lett.*, *27*, 2449–2452, doi:10.1029/2000GL000072.

Sauer, K., E. Dubinin, and K. Baumgärtel (1997), Bi-ion structuring in the magnetosheath of Mars—Theoretical modeling, *Adv. Space Res.*, *20*, 137., doi:10.1016/S0273-1177(97)00523-1.

Schunk, R., and A. Nagy (2000), *Ionospheres: Physics, Plasma Physics, and Chemistry*, pp. 88, 96–99, Cambridge Atmospheric and Space Science Series, Cambridge Univ. Press, Cambridge, U.K., New York.

Vasyliūnas, V. M. (2012), The physical basis of ionospheric electrodynamics, *Ann. Geophys.*, *30*, 357–369, doi:10.5194/angeo-30-357-2012.

Vignes, D., C. Mazelle, H. Rème, M. H. Acuña, J. E. P. Connerney, R. P. Lin, D. L. Mitchell, P. Cloutier, D. H. Crider, and N. F. Ness (2000), The solar wind interaction with Mars: Locations and shapes of the bow shock and the magnetic pile-up boundary from the observations of the MAG/ER experiment onboard Mars Global Surveyor, *Geophys. Res. Lett.*, *27*, 49–52, doi:10.1029/1999GL010703.

Withers, P. (2008), Theoretical models of ionospheric electrodynamics and plasma transport, *J. Geophys Res.*, *113*, A07301, doi:10.1029/2007JA012918.

Withers, P., M. Mendillo, H. Rishbeth, D. P. Hinson, and J. Arkani-Hamed (2005), Ionospheric characteristics above Martian crustal magnetic anomalies, *Geophys. Res. Let.*, *32*, L16204, doi:10.1029/2005GL023483.